International Journal of Fatigue 125 (2019) 406–417

Contents lists available at ScienceDirect

International Journal of Fatigue

journal homepage: www.elsevier.com/locate/ijfatigue

Improvement of low-cycle fatigue resistance in AISI 4140 steel by annealing treatment

M. Badaruddin[a,*], Sugiyanto[a], H. Wardono[a], Andoko[b], C.J. Wang[c], A.K. Rivai[d]

[a] Department of Mechanical Engineering, Faculty of Engineering, Universitas Lampung, Jalan Prof. S. Brojonegoro No.1., Bandar Lampung 35145, Indonesia
[b] Faculty of Engineering, State University of Malang, Jalan Semarang No. 5, Malang 65145, East Java, Indonesia
[c] Department of Mechanical Engineering, National Taiwan University of Science and Technology (NTUST), 43 Keelung Rd, Sec. 4, Taipei 106, Taiwan, ROC
[d] Center for Science and Advanced Material Technology, National Nuclear Energy Agency of Indonesia, Indonesia

ARTICLE INFO

Keywords:
AISI 4140 steel
Annealing treatment
Low-cycle fatigue
Near-Masing behaviour
Cyclic hardening

ABSTRACT

The low-cycle fatigue (LCF) behaviour of AISI 4140 steel under annealed and as-received conditions was investigated at room temperature. The annealing treatment causes a marked decrease in mechanical strength but an increase in plastic energy and ductility. The annealing treatment of AISI 4140 steel significantly increases the LCF resistance of the material. In addition, the steel exhibits a transitional behaviour from initial cyclic softening to stable cyclic hardening with increasing strain amplitude. By contrast, the as-received AISI 4140 steel undergoes progressive cyclic softening until failure. Microstructural changes induced in the annealed steel cause near-Masing-type behaviour at low and high strain amplitudes. The enhancement of the LCF resistance of the annealed steel is attributed to the high magnitude of the compressive stress, which is dependent on the applied strain amplitude. A good correlation of the total failure cycles with plastic strain and elastic strain provides a precise equation model for predicting the LCF life of annealing-treated AISI 4140 steel.

1. Introduction

In the automotive and aircraft industries, the strain-fatigue prediction of materials is widely accepted to determine the initial design of the industrial applications of components because the low cycle fatigue (LCF) behaviour of a material represents the actual loading condition of the component [1]. Regarding the application of a high-strength low-alloy (HSLA) medium carbon steel for machine components such as axles, driving shafts, gears, and stubs, AISI 4140 [1,2], micro-alloyed (MA) AISI 1141 [3], MA 8MnSiVS5 [4] and 34CrNiMo6 (AISI 4340) [5] steels are generally manufactured under quenching and tempering (Q&T) conditions. The Q&T heat-treatment to which these steels are subjected increases the mechanical strength of the steel and retains the appropriate ductility. These steels, which are composed of ferrite-martensite in the initial microstructure, are found to be very sensitive to cyclic plastic deformation [1–5], showing a gradual reduction in strength and cyclic softening behaviour until failure in low cycles. Paul et al. [6,7] have reported that dual-phase steel with high fraction volumes of up to 88% martensite undergoes progressive cyclic softening for all applied strain amplitudes until failure; however, steels with 20% and 49% volume fractions of martensite exhibit initial cyclic hardening and continuous cyclic softening at strain amplitudes higher than 0.5%. The dependence of ferrite-bainite microstructures on the LCF resistance is also observed in HSLA steels [8–10]. The initial cyclic hardening possibly results from the multiplication and interactions of dislocations in the initial microstructure [1–5]. Furthermore, the gradual dislocation rearrangement and the decrease in dislocation density are thought to cause cyclic softening after a few cycles of cyclic hardening [2,4,6–8,11]. Based on the brief literature above, HSLA steels with either ferrite-martensite or ferrite-bainite phases tend to experience different characteristics in terms of stress responses during strain-fatigue loading, depending on the applied strain amplitude.

In the present research, we focused on the improvement in the strain-fatigue life of AISI 4140 steel via annealing heat treatment. Numerous studies have focused on mechanical surface hardening by shot peening [12,13] and austempering heat treatment [14] on the high-cycle fatigue performance of AISI 4140 steel. However, the compressive residual stress from work hardening after shot peening contributes to a significant reduction in steel ductility [13,15], which is disadvantageous to LCF resistance; for example, the relaxation of residual stress during strain-fatigue loading in ferritic steel decreased slightly and the steel underwent cyclic softening after few loading cycles [15]. Furthermore, the austempered steel grades with a ferrite-bainite phase are known to have relatively low LCF resistance

* Corresponding author.
E-mail address: mbruddin@eng.unila.ac.id (M. Badaruddin).

https://doi.org/10.1016/j.ijfatigue.2019.04.020
Received 12 December 2018; Received in revised form 13 March 2019; Accepted 14 April 2019
Available online 15 April 2019
0142-1123/

[8–10,16]. HSLA steel grades with ferrite-pearlite microstructures are known to perform better in terms of strain-fatigue life [4,17]; however, a very low pearlite phase in the API-5L X65 steel causes the steel to undergo a gradual reduction in stress with fatigue cycles at all strain amplitudes [18]. Few publications on the LCF behaviour of annealed AISI 4140 steel are available in the literature, and the high strength of low-alloyed medium carbon steel with a ferrite-pearlite phase has been accepted as a replacement for the quenched and tempered steel grades in automotive and other applications [4]. Therefore, studying the influence of an annealing treatment on AISI 4140 steel is of great importance for improving the LCF properties of the steel. In the present research, the LCF behaviour of untreated and annealing treated AISI 4140 steel was investigated under strain-controlled cyclic loading at various strain amplitudes of 0.003–0.013 mm/mm at a constant strain rate of 0.005 s^{-1}. The characteristics of the softening and hardening behaviour and fractographical features of the specimens were studied. In addition, LCF properties were determined using the Coffin-Mansion-Basquin relationship.

2. Experimental procedures

2.1. Materials and specimens

In the present investigation, the original condition of a commercial AISI 4140 steel round is changed under quenching and tempering (Q&T). The chemical composition of this material is provided in Table 1. A steel specimen with a diameter of 16 mm and a length of 190 mm was subjected to annealing treatment at 815 °C in a box furnace for a 1 h holding time; then, the furnace temperature was decreased to 665 °C at a rate of 11 °C/min [19]. After the steel's temperature reached 665 °C, it was cooled to room temperature. Steel specimens that did not undergo this annealing treatment were symbolized as-received steel (RS), and steel that did undergo this annealing treatment was symbolized as annealed steel (AS). Tensile test specimens were prepared according to the ASTM E8 standard [20] (Fig. 1a), and smooth cylindrical specimens for LCF tests were prepared according to the ASTM E606 standard [21] (Fig. 1b).

2.2. Tensile and LCF tests

Both static tensile and LCF tests were carried out using a computerize servohydraulic MTS Landmark 100 kN at room temperature. The tests were run using different template programs in MTS multipurpose elite (MPE) software. Two of each of the RS and AS specimens were tested under axial loading to investigate their mechanical properties. The 50 mm gage length of an axial extensometer (MTS 634.25F- 24 type) was attached in the gage length area of a specimen. The specimen was axially pulled at a constant speed of 0.2 mm/min until it broke. The resultant stress data and strain (from the extensometer measurements) data were plotted in the form of the stress-strain curve.

In the LCF tests, ten annealed and as-received specimens were fatigued under full reversed triangular wave loading ($R_\varepsilon = -1$) controlled by an MTS 623.12F-20 type axial extensometer with a 10 mm gage attached in the gage length area. The LCF tests used various strain amplitudes of 0.003–0.013 mm/mm applied at a constant strain rate of 0.005 s^{-1}. The frequencies for the LCF tests were calculated using the equation in Ref. [22], which were 0.417 Hz, 0.25 Hz, 0.179 Hz, 0.139 Hz, 0.114 Hz and 0.096 Hz for 0.003 mm/mm, 0,005 mm/mm, 0.007 mm/mm, 0.009 mm/mm, 0.011 mm/mm and 0.013 mm/mm strain amplitudes, respectively. In the present experiment, the failure cycle was investigated at a load drop of 50% of the stable cycle. Plastic strain, elastic strain and elastic moduli data were measured at half cycles ($0.5N_f$) during the LCF tests. Pairs of data points consisting of plastic strain and elastic strain with reversals to failure cycles ($2N_f$) at all the tested strain amplitudes were plotted to determine LCF parameters using the Coffin–Manson-Basquin relationship.

Table 1
Chemical composition of the as-received AISI 4140 steel (wt.%).

C	Mo	Mn	Cr	Si	P	S
0.443	0.198	0.805	1.150	0. 308	0.021	0.010
Ni	Al	Co	Cu	Ti	W	Fe
0.253	0.0198	0.020	0.320	0.026	0.0114	Bal.

The microstructures of the as-received AISI 4140 steel and the AS were observed by means of an optical Olympus microscope after metallographic grinding and polishing followed by etching with 2% nital. Morphologies of the fracture surface of the RS and AS samples tested for LCF at all the tested applied strain amplitudes were described by means of scanning electron microscopy (SEM) with secondary electron image (SEI) signals (SEM Carl Zeiss EVO MA 10).

3. Results and discussion

3.1. Microstructures

The microstructure of the as-received AISI 4140 steel is shown in Fig. 2a. Small ferrite grains and fine martensite are observed in the microstructure, which consist of cementite (Fe_3C) and ferrite. The dark particles are possibly small clusters of cementite globular rather than precipitates, reflecting a microstructure similar to that reported in Ref. [13,23]. The diffusion of carbon atoms into the martensite during high-temperature tempering inhibited by chromium grows cementite particles in globular shapes [24].

The typical microstructure of an annealed sample is displayed in Fig. 2b. The typical shapes of the proeutectoid coarse ferrite grains and the coarse pearlite grains are shown in Fig. 2b. Pearlite colonies contain cementite lamellae, which is clearly observed as a second phase precipitate in the ferrite matrix, and the ferrite and lamellar layers vary from grain to grain in terms of thickness; some of the pearlite appears dark because the layers are close together and cannot be clearly observed under the magnification of the photomicrograph. This microstructure is similar to that of annealed AISI 4140, which was examined using X-ray diffraction and transmission electron microscopy (TEM) in the literature [14].

3.2. Mechanical properties

The typical stress-strain curves for the AISI 4140 steel with and without undergoing the annealing treatment are depicted in Fig. 3. The elastic modulus (E) of the steel was determined by means of plotting the linear elastic curve with a segment line length of 20% in the range of the linear stress-strain relationship using the least-squares regression method [20]. Yield strength, σ_y, was calculated using the 0.2% offset method. The tensile test results are summarized in Table 2. It is clear that the microstructural changes induced by the heat treatment of the AISI 4140 steel (Fig. 2a and b) significantly affect the mechanical strength of the steel (Fig. 3). The carbon mass fraction of ~0.443% in the as-received AISI 4140 steel is more than enough to result in the large volume fraction of martensite via interstitial carbon atoms in the body-centred tetragonal (BCT) martensite, which results in more martensite particles in the form of a solid solution in the ferrite matrix. In addition, the small Fe_3C particles that precipitate in the martensite phase can reinforce the ferrite [2,25]. Small ferrite grains and fine martensite dispersions (in Fig. 2a) provide a large ferrite-martensite phase boundary area. Thus, the available phase boundary area can serve as a barrier to dislocation movement, which substantially enhances the strength. Medirata et al. [11] have reported similar characteristics in C-Mn-Si dual-phase steel. The ductility of ferrite accounts for the improvement in the ductility of the AISI 4140 steel in Q&T conditions (Fig. 3).

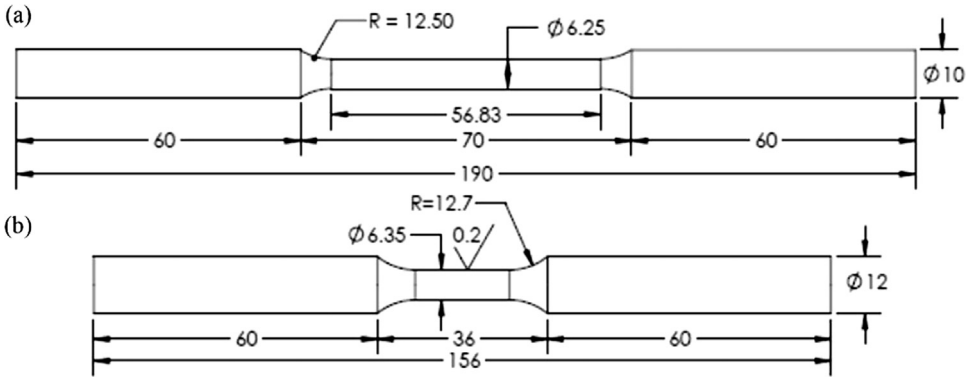

Fig. 1. Details of the specimens: (a) tensile test and (b) LCF test (units in mm).

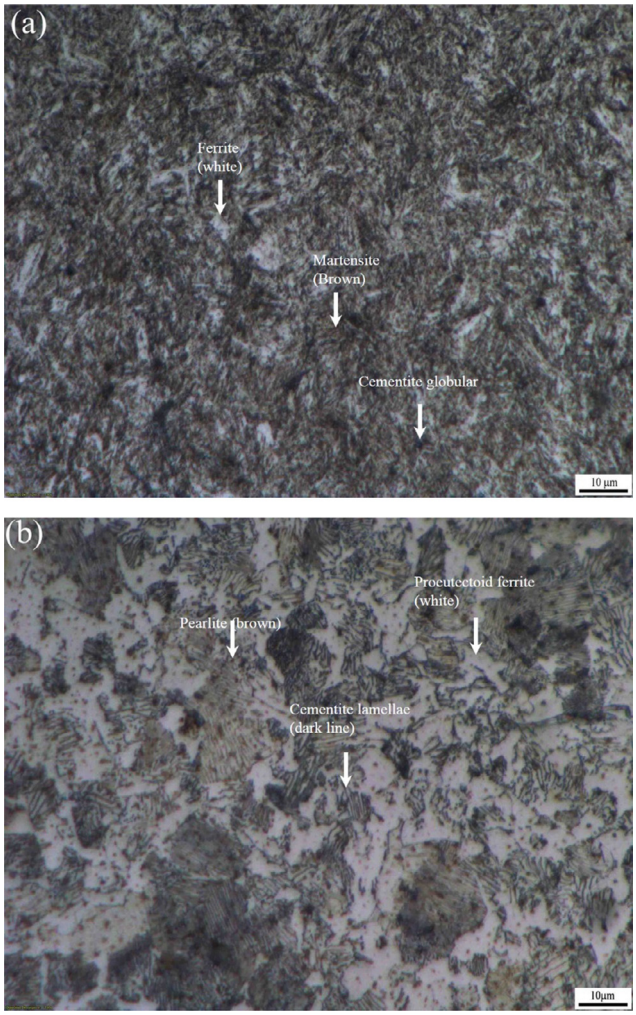

Fig. 2. (a) Initial microstructure of the as-received AISI 4140 and (b) the microstructure of the AS.

Even though the annealing treatment of AISI 4140 steel reduces the mechanical strength, ultimate strength (σ_{ult}) and yield strength (σ_y) of the steel, ductility and plastic energy increase significantly. The mass fractions of pearlite and proeutectoid ferrite, which are 57.05% and 42.95%, respectively, can be determined by the lever rule and tie line methods. Thus, a higher fraction of pearlite in the AS will result in a significant material strength enhancement (Table 2). Cieslak et al. [17] reported a similar finding for the microstructure of R260 steel that consists of a pearlite phase with randomly oriented lamellar in the interior of the grain. In addition, as shown in Fig. 2b, the relative

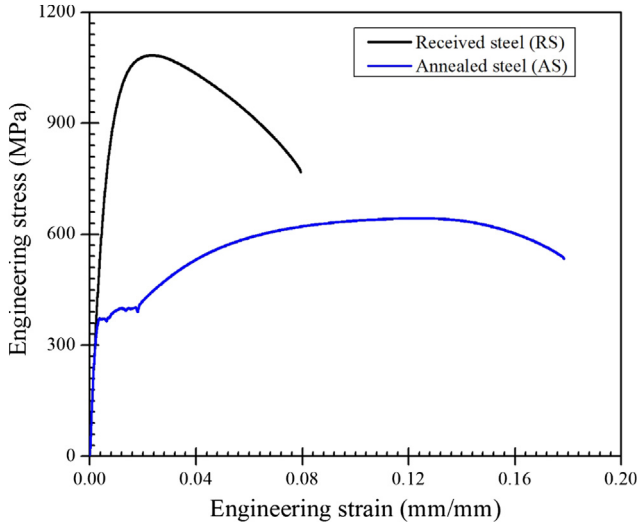

Fig. 3. Typical stress-strain curve for the as-received AISI 4140 steel and the annealed AISI 4140 steel.

Table 2
Tensile test results.

Material	*σy* (MPa)	*σult* (MPa)	Ep (kJ)	*Ee* (kJ)	E (GPa)	*e* (%)
The as-received AISI 4140	939.52	1093.69	0.001	0.028	209.88	14.60
Annealed steel	384.97	666.86	0.087	0.002	205.53	21.00

Table 3
Typical strain-life LCF results for both as-received AISI 4140 (RS) and annealed steel (AS).

Material	$\Delta\varepsilon_t$ (mm/mm)	ε_a (mm/mm)		E (GPa)	N_f (cycles)	σ_a (MPa)
		ε_{ap}	ε_{ae}			
RS1	0.003	0.00015	0.0029	194.99	18,563	548.50
RS2	0.005	0.0015	0.0035	193.50	3161	634.00
RS3	0.007	0.0035	0.0035	193.03	1000	716.00
RS4	0.009	0.0050	0.0040	192.36	604	733.00
RS5	0.011	0.0070	0.0040	192.25	405	807.00
RS6	0.013	0.0085	0.0045	193.81	166	860.50
AS1	0.003	0.0015	0.0015	207.10	26,858	333.00
AS2	0.005	0.0031	0.0019	202.07	3606	381.50
AS3	0.007	0.0049	0.0021	202.06	1912	436.50
AS4	0.009	0.0066	0.0025	198.27	733	464.50
AS5	0.011	0.0085	0.0025	200.25	415	498.00
AS6	0.013	0.0105	0.0025	195.46	336	516.50

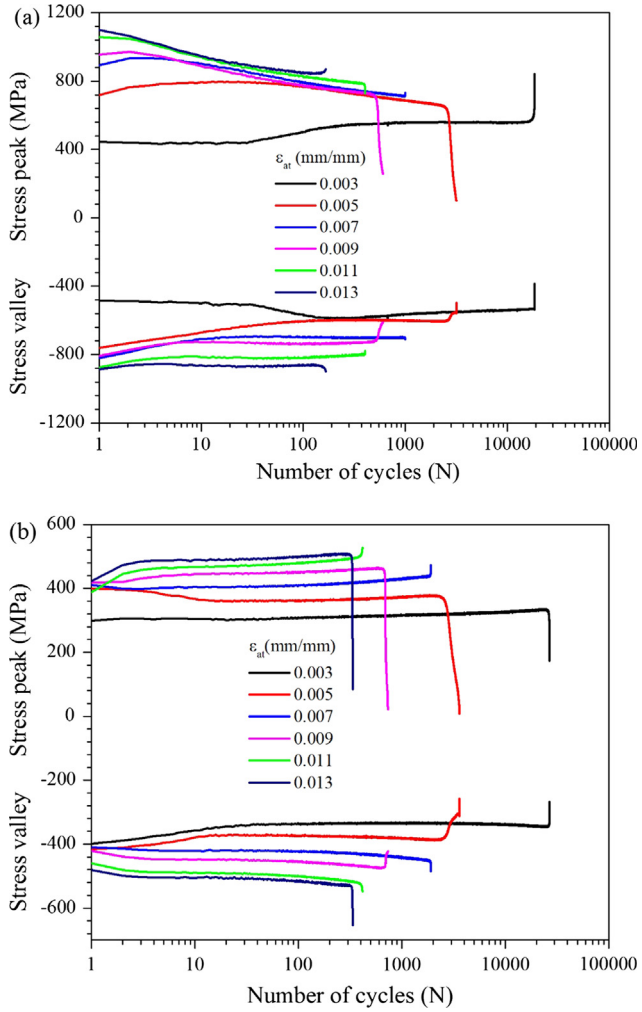

Fig. 4. Cyclic stress response during LCF tests: (a) the as-received AISI 4140 steel and (b) AS.

thicknesses of the ferrite and lamellar layers in the microstructure is one of the reasons for the relatively high ductility of AS.

3.3. Cyclic stress response analysis

The LCF test results are displayed in Table 3. The average values of the elastic modulus for the annealed and as-received AISI 4140 steel are 200.87 GPa and 193.32 GPa, respectively. The different elastic modulus values obtained from static tensile testing and LCF testing (Tables 2 and 3) are possibly caused by the decrease in the microplastification connections with the reversible movement of dislocations and the decrease in the formation of Lüders bands [26].

The influences of the strain amplitude on the cyclic stress responses with respect to the number of cycles at a constant strain rate of $0.005\ s^{-1}$ are depicted for each steel in Fig. 4a and b. The stress peak response of the AISI 4140 steel increased with strain amplitude (Fig. 4a). In contrast, the AS exhibits an identical cyclic stress response at higher strain amplitudes (Fig. 4b). At lower strain amplitudes, the differences in the cyclic stress responses at peak stress (tension) and valley stress (compressive) of specimen AS1 to those of specimen RS1 are approximately 150 MPa and approximately 100 MPa. Specimen RS1 showed continuous slight cyclic softening behaviour for 30 cycles, and progressive cyclic hardening behaviour was observed from the 1000th cycle until the steel underwent saturation cyclic hardening and ultimately failed. In addition, a slight increase in the magnitude of the compressive stress was observed from 1 to 1000 cycles. When the strain amplitudes were increased (0.005–0.009 mm/mm), the as-received AISI 4140 underwent initial cyclic hardening for two cycles.

Fig. 4a clearly shows the initial cyclic hardening and continuous cyclic softening behaviours of the as-received AISI 4140 steel under Q&T conditions, which are strongly correlated with the relatively high portion of martensite in the initial microstructure (Fig. 2a). Similar behaviour was generally found in many HSLA medium carbon steels, such as dual-phase (ferrite-martensite) steel [6,7], CrMoV steel [8], and a carbide-free bainitic steel [10,16,17], the microstructures of which have more martensite phases than ferrite phases. The low plastic deformation of martensite on cyclic straining has been reported in the literature [2,6,7,10]. The martensite phase has highly effective interstitial carbon, which results in the hardest, strongest, and most brittle phase; therefore, the phase has relatively few slip systems for dislocation motion for the BCT structure [27]. When the strain amplitude was increased to 0.011 mm/mm and 0.013 mm/mm, the AISI 4140 steel continued to experience significant cyclic softening behaviour, indicating that the steel was not capable of cyclic deformation (Fig. 4a). In contrast, specimen AS1 exhibited initial cyclic hardening until 8 cycles of loading, and with loading from 9 to 20 cycles, specimen AS1 underwent cyclic softening behaviour (Fig. 4b). After the 21st cycle, specimen AS1 experienced cyclic hardening until failure. When the strain amplitudes were increased to 0.007 mm/mm, the AS underwent cyclic softening within a few cycles and continuous cyclic hardening until failure.

The identical stress peak at a higher strain amplitude of 0.003 mm/mm, which was observed for the AS at the first loading cycle, was related to the serration yield strength phenomenon, which is evident in Fig. 3. This phenomenon was similar to that observed in 42CrMo4 steel (AISI 4140 steel) under normalizing conditions [28]. After the AS experienced the serration phenomenon, cyclic hardening occurred in the steel at a higher strain amplitude of 0.005 mm/mm (Fig. 4b). The few cyclic softening cycles observed at a low strain amplitude of 0.005 mm/mm are possibly due to the formation of low plastically deformed zones in the Lüders band regions, where the free dislocation regions are active [28,29]. Conversely, the cyclic hardening is thought to be due to the extensive work hardening that resulted from increasing the dislocation cell structure in proeutectoid ferrite and the interaction dislocations of cementite lamellae in coarse pearlite. In this present study, AISI 4140 steel under annealing conditions underwent cyclic softening in a few cycles and then underwent stable cyclic hardening until failure with the increasing strain amplitude, similar to low carbon steel [30] and medium carbon hot-forged MA 49MnVS3 steel [4,29], which have more of the pearlite phase. Sarma et al. [29] verified the mechanism of cyclic softening and stable cyclic hardening by a transmission electron microscope (TEM) examination of hot-forged MA medium carbon steel (49MnVS3 steel grade) after LCF at a strain amplitude of 0.8%.

3.4. Cyclic stress-strain behaviour

Fig. 5a and b show a typical plot of the hysteresis loops for the as-received AISI 4140 at different strain amplitudes. The evolution of the hysteresis curve in Fig. 5a shows that the steel cyclically softens for 30 cycles and experiences a slight increase in compressive stress, which indicates that the steel undergoes some work hardening; consequently, the steel exhibits a gradual increase in cyclic hardening for 100 cycles. Stable cyclic hardening, which is clearly observed for 1000 cycles, is followed by cyclic softening until the steel fails. Furthermore, at a higher strain amplitude of 0.007 mm/mm, the steel behaviour evidently underwent cyclic hardening from the 2nd to 10th cycles, followed progressive cyclic softening with a decreased peak stress and an increased number of cycles (Fig. 5b).

To investigate the cyclic softening and hardening behaviours the hysteresis loops at a 0.011 mm/mm strain amplitude, 1, 2, 10, 20, 50, 100, 200, 300 and 400 cycles were examined (Fig. 6a and b). It is clear from Fig. 6a that the decrease in the linear portion of the hysteresis loop

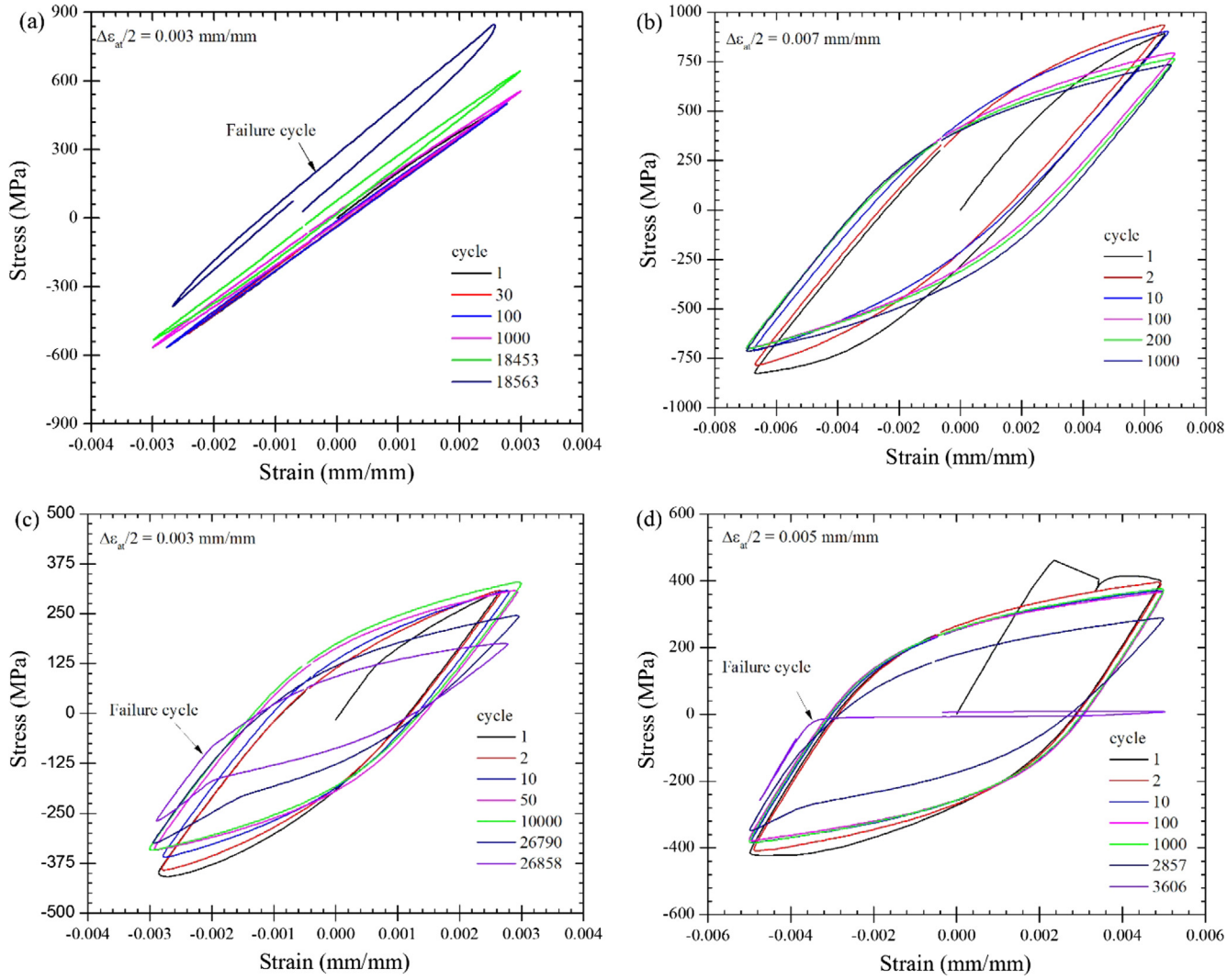

Fig. 5. Plots of the hysteresis loops obtained from the LCF tests at different strain amplitudes: (a and b) the as-received AISI 4140 and (c and d) the AS.

indicates cyclic softening for the as-received AISI 4140 steel. Thielen et al. [2] observed dislocations in the ferrite-martensite microstructure of the quenched and tempered AISI 4140 steel after cyclic strain fatigue at a 1% and a 2.5% strain amplitudes using TEM; the rearrangement of the dislocation and reduction of the dislocation density were caused by the highly inhomogeneous dislocation arrays in the dislocation-free regions, which led to cyclic softening. In addition, the very low number of carbide precipitates in the small ferrite grains due to the low number of carbon atoms is possibly unable to anchor slip deformations, which enables the as-received AISI 4140 steel to undergo continuous cyclic softening with increasing cycle fatigue, which is evident in Fig. 5b.

Furthermore, Fig. 5c and d show the influence of the annealing treatment on the present AISI 4140 steel, which significantly changes the behaviour of the steel during cyclic deformation. Pearlite consisting of a large number of cementite lamellae precipitates (Fig. 2b) is thought to cause the cyclic hardening behaviour of the annealed AISI 4140 steel. The evolution of the hysteresis loops shows the increase in the linear portion of the loading paths (Fig. 6b), which indicates that the AS clearly undergoes cyclic hardening.

Typical microstructures of a sample tested at a strain amplitude of 0.009 mm/mm were characterized by optical microscopy for the RS; annealing conditions are displayed in Fig. 7a and b, respectively. The microstructure of the as-received AISI 4140 does not show a significant change in grain size and no deformed trace grains can be observed in the microstructure (Fig. 7a). By contrast, deformed cementite lamellae can be observed; bending and kinking cementite shapes in the pearlite regions are clearly seen in Fig. 7b, which indicates that significant plastic deformation occurs in the AS. The plastic deformation of the cementite in the pearlite regions occurred due to compressive loading and resulted in the bending and kinking of cementite lamellae. A similar characteristic was observed by TEM observation of the microstructure of hot-forged 49MnVS3 steel that was cyclically strain fatigued at a 0.8% strain amplitude [29]. In addition, the grains of proeutectoid ferrite and pearlite in the microstructure of the AS show significant reductions in size after cyclic fatigue deformation (Fig. 7b). This observation is similar to observations in previous investigations reported by Kreethi et al. [31]; the average grain size of AISI 4140 steel decreased up to 17.27% under annealing conditions.

To quantify the variations in softening or hardening related to an increase in the strain amplitude, the cyclic softening ratio (S) and hardening ratio (H) are calculated using Eq. (1):

$$S \text{ or } H = \left[\frac{\sigma_{p(N=0.5N_f)} - \sigma_{p(N=1)}}{\sigma_{p(N=1)}} \right] \quad (1)$$

where $\sigma_{p(N=1)}$ and $\sigma_{p(N=0.5N_f)}$ are the stress peaks at the first cycle and at the half-life cycle, respectively. In Eq. (1), the minus sign indicates softening, and the positive sign indicates hardening. Fig. 8 shows the variations in S and H with different strain amplitudes. The softening ratio significantly decreases with increasing strain amplitude for the as-

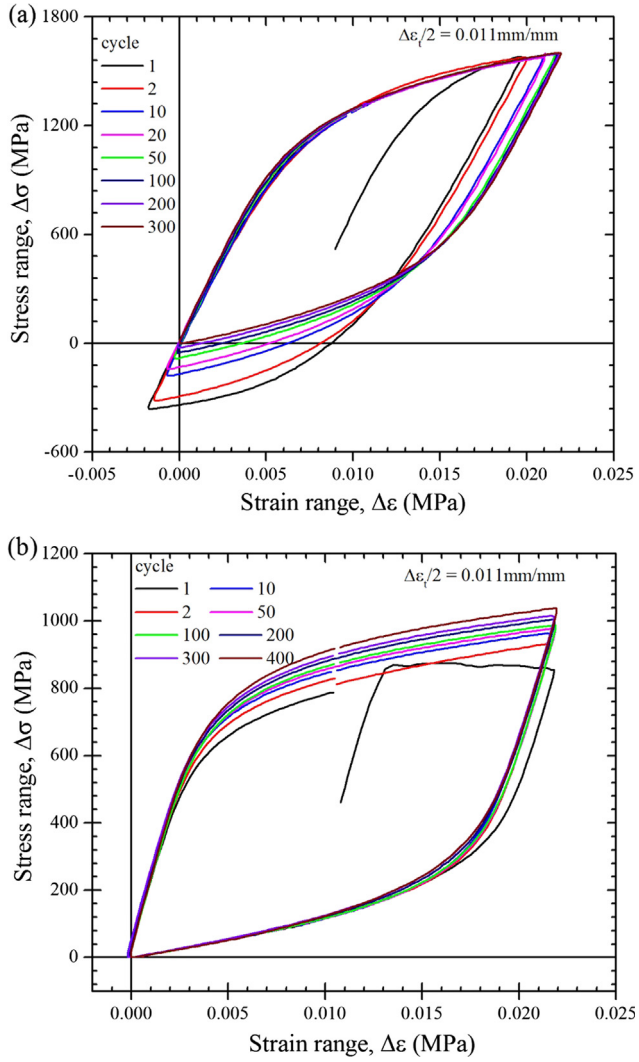

Fig. 6. Plots of the hysteresis loops with matching upper branches during symmetrical strain cycling with a strain amplitude of 0.011 mm/mm: (a) the as-received AISI 4140 steel and (b) the AS.

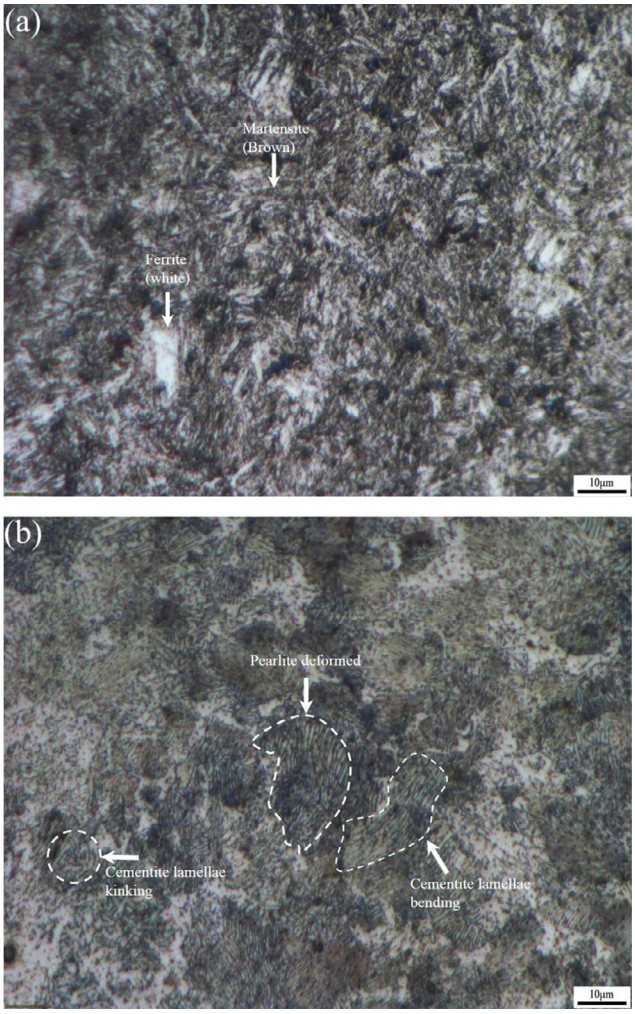

Fig. 7. Optical micrograph of (a) an RS sample and (b) an AS sample after LCF testing at a strain amplitude of 0.009 mm/mm.

received AISI 4140 steel. In addition, strain amplitudes of 0.005 mm/mm and 0.011 mm/mm show the saturation points where the AS experienced a transition from cyclic softening to hardening. The softening/hardening ratio of the AS forms an S-shaped curve.

3.5. Masing and non-Masing behaviour

The expression of Masing and non-Masing behaviour depends on the specimen microstructure and the experimental cyclic straining condition [5], which can be observed via the cyclic stress-strain response at half-life cycle conditions. Generally, Masing behaviour suggests that the plastic deformation or the effective obstacle dislocation movement is relatively constant with increasing strain amplitude. In contrast, the change in structural deformation from planar slip to formation of a cell structure suggests non-Masing behaviour in a material, which is dependent on any given strain amplitude [32]. To describe the Masing and non-Masing behaviour [18], the hysteresis loops corresponding to different strain amplitudes of the LCF tests at the half-life cycle are shifted to a common origin by subtracting the stress and the strain components with the maximum compressive stress and the maximum compressive strain, as shown in Fig. 9a and b.

Material exhibits Masing behaviour if the loading paths at the half cycles coincide at different strain amplitudes [5,18]. On the other hand,

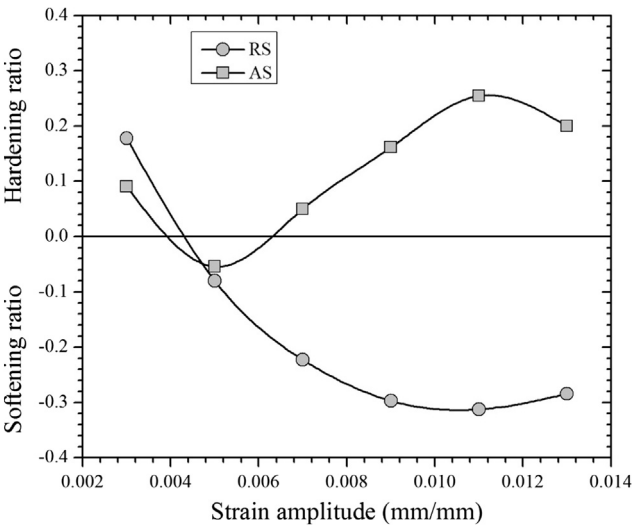

Fig. 8. The cyclic softening/hardening ratios of the RS and AS from the LCF tests at a constant strain rate of 0.005 s^{-1}.

a material does not experience non-Masing behaviour when the hysteresis loops do not share a loading path. Fig. 9a clearly shows that the as-received AISI 4140 steel at any given strain amplitude does not exhibit Masing-type behaviour. However, the AS results at strain

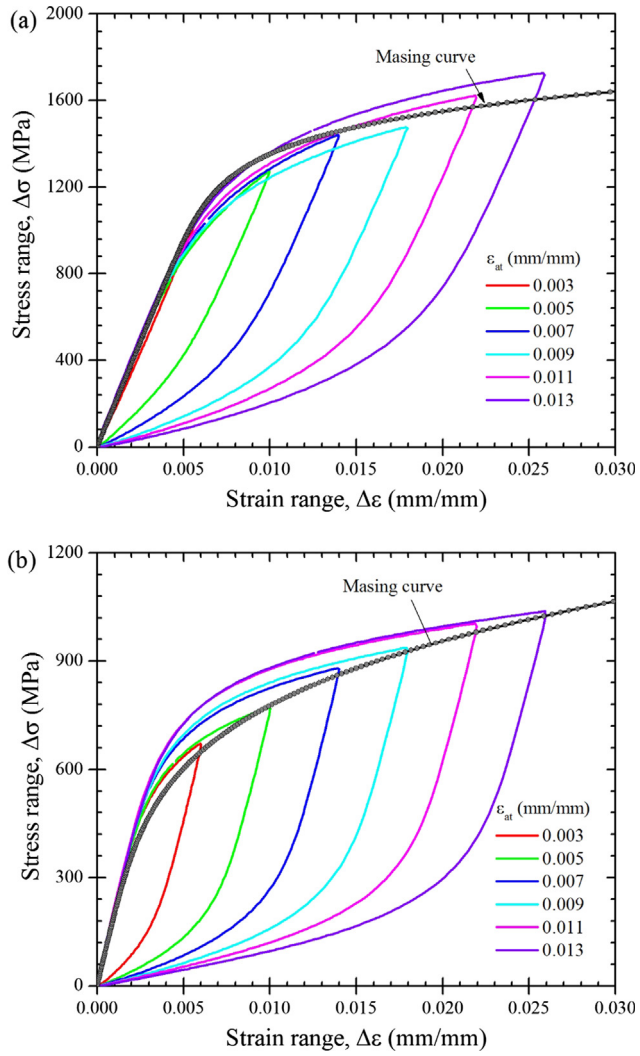

Fig. 9. The non-Masing and near-Masing curves superimposed on hysteresis loops at half cycles with a common compressive tip for (a) the as-received AISI 4140 and (b) AS.

amplitudes of 0.003 mm/mm and 0.011 mm/mm are somewhat coincident with those at strain amplitudes of 0.005 mm/mm and 0.013 mm/mm steel (Fig. 9b), respectively. The small divergence in deviation from an ideal Masing-type behaviour shows that the AS exhibits near-Masing-type material behaviour, which is similar to findings reported by Sarkar et al. [32] in the literature. Thus, the annealing treatment resulted in a change from non-Masing-type behaviour to near-Masing-type behaviour at low and high strain amplitudes.

3.6. Strain based on fatigue life analysis

The relationship between the stress amplitude ($\Delta\sigma/2$) and total strain amplitude ($\Delta\varepsilon_t/2$) is an important factor in investigating a material that undergoes strain hardening due to cyclic loading. The cyclic stress-strain equation can be described by Eq. (2):

$$\Delta\varepsilon_t = \frac{\Delta\epsilon_e}{2} + \frac{\Delta\varepsilon_p}{2} = \frac{(\Delta\sigma)}{2E} + \left(\frac{\Delta\sigma}{2K'}\right)^{\frac{1}{n'}} \tag{2}$$

where $\Delta\varepsilon_e/2$ and $\Delta\varepsilon_p/2$ are the elastic strain amplitude and the plastic strain amplitude, respectively. E is the elastic modulus under cyclic conditions. The plastic term of Eq. (2) can be written as follows:

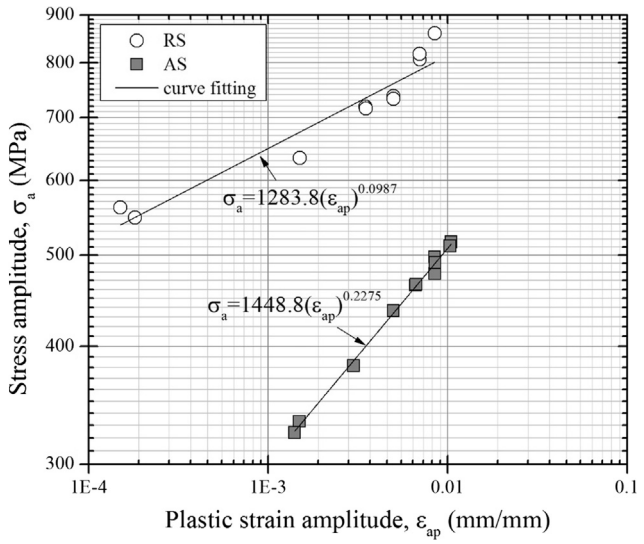

Fig. 10. Influence of annealing treatment on the cyclic stress amplitude and the plastic strain amplitude obtained from the LCF tests at different strain amplitudes.

$$\frac{\Delta\sigma}{2} = K'\left(\frac{\Delta\varepsilon_p}{2}\right)^{n'} \tag{3}$$

where K' is the cyclic strength coefficient and n' is the cyclic strain hardening exponent. A log-log plot of $\Delta\sigma/2$ versus $\Delta\varepsilon_p/2$ from the hysteresis loops at the half cycles obtained from the LCF data at different strain amplitudes is displayed in Fig. 10. The values of K' and n' were determined from the linear fitting regression in Fig. 10 and tabulated in Table 4.

The Coffin–Manson–Basquin equation is always used to predict the fatigue life of a material based on a strain-controlled LCF test and is represented by Eq. (4) [21].

$$\Delta\varepsilon_t = \frac{\sigma_f'}{E}(2N_f)^b + \varepsilon_f'(2N_f)^c \tag{4}$$

This equation is the result of a combination of the equations for the elastic component and the plastic component developed by Basquin and Coffin–Manson [21], as given by Eqs. (5) and (6), respectively.

$$\frac{\Delta\varepsilon_e}{2} = \frac{\sigma_f'}{E}(2N_f)^b \tag{5}$$

$$\frac{\Delta\varepsilon_p}{2} = \varepsilon_f'(2N_f)^c \tag{6}$$

Furthermore, the LCF steel parameters can be determined through a curve fitting method by plotting pairs of the plastic and elastic strain components from the experimental data with the number of reversals to failure (2Nf) at a log-log scale. The LCF parameters for the as-received AISI 4140 steel and AS are summarized in Table 4. The total strain versus reversals to failure based on these parameters is plotted in Fig. 11a and b for the as-received AISI 4140 and AS, respectively, and the curves show a good correlation with the experimental data.

In the present study, the fatigue strength coefficient ($\sigma_f' = 1432.9$ MPa) and the fatigue strength exponent ($b = -0.0992$) of the as-received AISI 4140 steel under Q&T conditions are identical to those of the quenched AISI 4140 steel tempered at a temperature of 650 °C reported by Thielen et al. [2] and dual-phase steel with 45.42% martensite [33]. The value of b is generally observed to be in a range of $-0.111 < b < -0.070$ for the HSLA of medium carbon steels under Q&T conditions [3,8,11]. The fatigue ductility coefficient ($\varepsilon_f' = 1.2482$ mm/mm) and the fatigue ductility exponent ($c = -0.8777$) are nearly identical to those of the AISI 1141 steel and

Table 4
LCF properties for as-received AISI 4140 steel and annealed steel.

Parameters	The as-received AISI 4140 steel	The annealed steel
Cyclic strength coefficient, K' (MPa)	1283.8	1448.8
Fatigue strength coefficient, σ_f' (MPa)	1432.9	1030.8
Cyclic strain hardening exponent, n'	0.0986	0.2275
Fatigue strength exponent, b	−0.0992	−0.1202
Fatigue ductility coefficient, ε_f' mm/mm	1.2482	0.1297
Fatigue ductility exponent, c	−0.8777	−0.4437

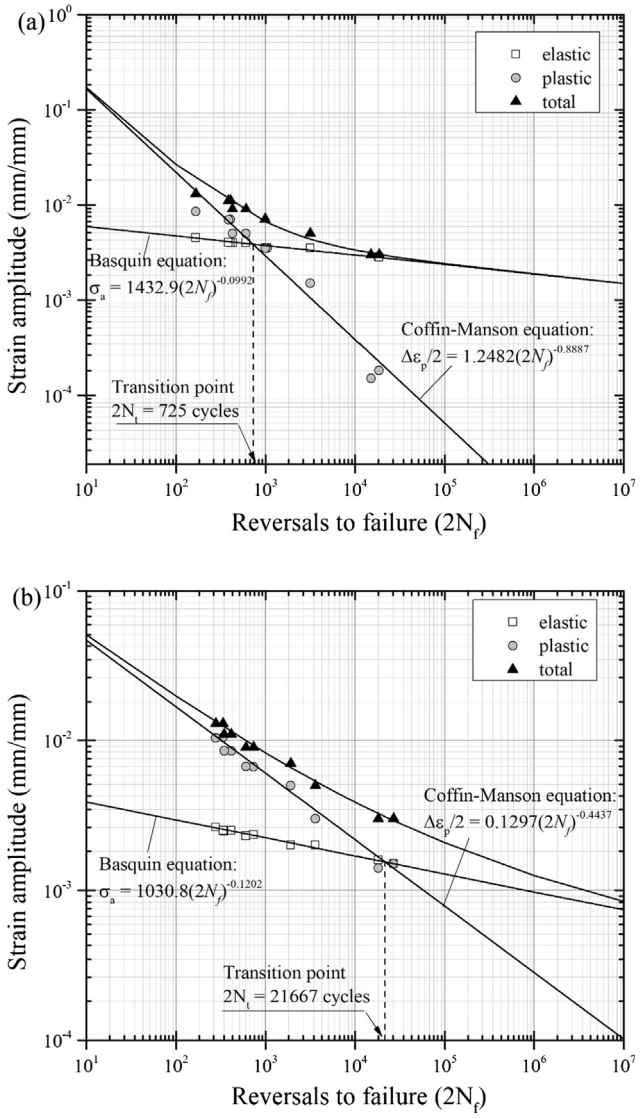

Fig. 11. Fatigue strain-life curves and calibration curves using the Coffin–Manson–Basquin relationship for (a) the as-received AISI 4140 steel and (b) the AS.

the C-Mn-Si dual-phase steel under Q&T conditions reported by Fatemi et al. [3] and Mediratta et al. [11], respectively, and the ε_f' and c values are slightly greater than those reported in the literature [2,4,8].

The value of ε_f' for the as-received AISI 4140 steel under Q&T is higher than that of the AS. This phenomenon was generally found for the HSLA medium carbon steels, for which the elastic strain is sometimes higher than the plastic strain at low strain amplitudes [4,11,34]. In the present investigation, the improvement in the LCF resistance of the AISI 4140 steel under annealing conditions may be correlated with the low fatigue ductility exponent (c) and the highly cyclic strain hardening exponent (n').

As displayed in Table 4, the cyclic strain hardening exponent (n' = 0.2275) of the AS is higher than that of the as-received AISI 4140 steel (n' = 0.0987). The low value of n' for the as-received AISI 4140 steel can be correlated with the relatively high fraction of the martensite phase in the microstructure of the steel [27,33]. The respective values of n' = 0.2275 and c = −0.4437 for the annealed AISI 4140 steel are comparable to those reported for other HSLA medium carbon steels in hot-forged manufacturing [3,4,11]; thus, the AISI 4140 steel under annealing conditions is better than that of Q&T steel grades in terms of LCF behaviour. The high n' value shows that the annealed AISI 4140 steel can accommodate significant plastic deformation during cyclic strain fatigue, which results in the progressive work hardening indicated by the high magnitude of the compressive stress (Fig. 4b). Materials with high magnitudes of compressive stress can achieve high plasticity at the crack tip even though the stress concentration is high [8]. The predictions of fatigue life for the as-received AISI 4140 steel and the AS in terms of the elastic and plastic components, using the Basquin and Coffin–Manson approaches, respectively, are as follows.

For the as-received AISI 4140 steel:

$$\sigma_a = 1432.9(2N_f)^{-0.0992} \tag{7}$$

$$\frac{\Delta\varepsilon_p}{2} = 1.2482(2N_f)^{-0.8777} \tag{8}$$

For the annealed AISI 4140 steel:

$$\sigma_a = 1030.8(2N_f)^{-0.1202} \tag{9}$$

$$\frac{\Delta\varepsilon_p}{2} = 0.1297(2N_f)^{-0.4437} \tag{10}$$

The number of transition cycles (N_t) can be determined by substituting the values of $\varepsilon_{ae} = \varepsilon_{ap}$ and replacing $2N_f$ with $2N_t$ from Eqs. (7) to (10). The number of transition cycles ($2N_t$) for the as-received AISI 4140 steel and AS are 725 cycles and 21,677 cycles, respectively. When $2N_f \gg 2N_t$, the elastic strain is more dominant in controlling the fatigue performance of the material. In contrast, when $2N_f \ll 2N_t$, the plastic strain dominantly controls the fatigue performance. The high magnitude of cyclic compressive stress resulted from the work hardening of AS can be seen as an important factor for determining the effectiveness of fatigue performance improvement. The significant effect of transition life on the fatigue strength of steel can be correlated to compressive residual stress and hardness [35,36]. The compressive stress that results from plastic deformation during cyclic loading, which benefits the fatigue performance of the material, is identical to the residual stress at the surface of the material due to mechanical surface hardening [12,37].

3.7. Plastic strain energy based on LCF prediction

Because LCF damage is associated with cyclic plastic strain, the plastic strain energy can be considered for an accurate prediction of the fatigue life of a material. The dissipation energy absorbed by a material during cyclic fatigue damage can be employed for predicting its LCF lifetime via the plot of plastic strain energy (MJ/m^3) with the reversals

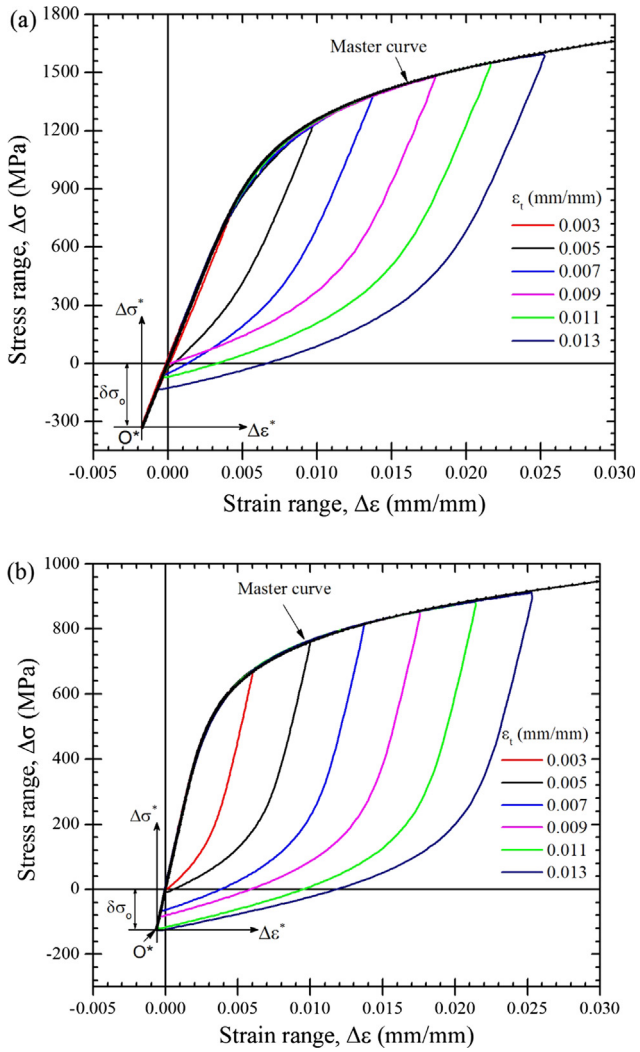

Fig. 12. Master curve constructions for (a) the as-received AISI 4140 steel and (b) AS.

to failure ($2N_f$). For a material exhibiting non-Masing behaviour (Fig. 9a and b), the concept of a 'master curve' can be introduced by matching each path of the tensile branch for all the strain amplitudes along their linear elastic portions [18]. Eq. (11) can be applied to create the master curve, expressed as [38]:

$$\frac{\Delta\varepsilon^*}{2} = \frac{\Delta\sigma^*}{2E} + 2\left(\frac{\Delta\sigma^*}{2K^*}\right)^{\frac{1}{n^*}} \tag{11}$$

Furthermore, the dissipation plastic strain energy per cycle is calculated using Eq. (12) [38].

$$\Delta W_p = \left(\frac{1-n^*}{1+n^*}\right)\Delta\sigma\Delta\varepsilon_p + \left(\frac{2n^*}{1+n^*}\right)\delta\sigma_o\Delta\varepsilon_p \tag{12}$$

where K^* and n^* correspond to the master curve parameters measured with respect to the new origin (O^*) in Fig. 12a and b. These values were obtained from fitting of the experimental data. The relationships between the old and new coordinate systems, as shown in Fig. 12, are available in the literature [5,18]. In the present experiment, the K^* and n^* values are 3015.4 MPa and 0.1547 for the as-received AISI 4140 steel, respectively, and for the AS, the K^* and n^* values are 1677.3 MPa and 0.1557, respectively. A value of $\delta\sigma_o$ can be measured from Fig. 12a and b. Furthermore, the plastic strain energy (ΔW_p) was calculated using Eq. (12). The LCF properties based on plastic strain energy can be determined using the Coffin–Manson power law relationship [5,22] by

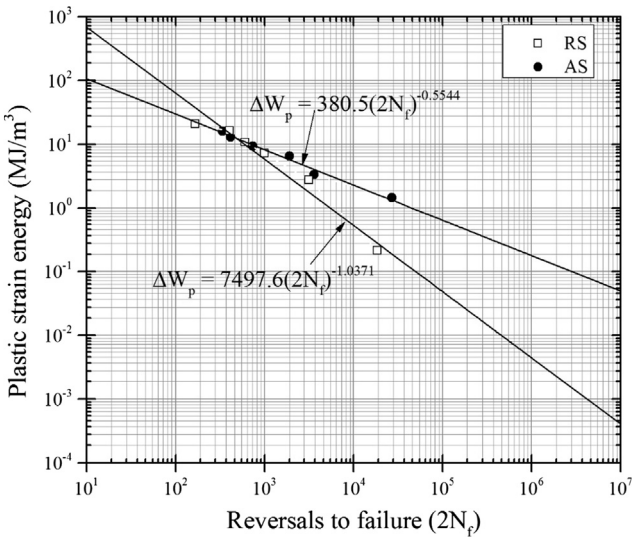

Fig. 13. LCF plots based on plastic strain energy with reversals to failure (2Nf) for strain amplitudes ranging from 0.003 to 0.013 mm/mm.

Table 5
LCF parameters based on plastic strain energy.

Material	$W_f^{'}$	ω
The as-received AISI 4140 steel	7497.6	−1.0371
The annealed steel	380.5	−0.5544

using Eq. (13):

$$\Delta W_p = W_f^{'}(2N_f)^{\omega} \tag{13}$$

where $W_f^{'}$ and ω are the plastic strain energy coefficient and the plastic strain energy exponent, respectively, where ω is the sum of b and c. The plot of ΔW_p versus reversals to failure ($2N_f$) is shown in Fig. 13, and the LCF parameters are presented in Table 5. In this experiment, the annealing treatment on the as-received AISI 4140 steel tested under LCF conditions with strain amplitudes ranging from 0.003 to 0.013 mm/mm decreased both the $W_f^{'}$ and ω values. A similar effect of the annealing treatment on the decrease in the values of $\varepsilon_f^{'}$ and c determined by the Coffin–Manson relationship is shown in Fig. 11b. The values of ω obtained for the as-received AISI 4140 and AS are very close to the sum of the values of b and c in Table 4.

3.8. Fractographical observation

The SEM fractography of Fig. 14 displays a typical surface fracture of the RS and AS samples tested under LCF at 0.009 mm/mm strain amplitudes; crack initiation due to the persistent slip bands near the specimen surface can be observed in Fig. 14a and d. A close analysis of the RS and AS samples in Fig. 14b and e shows cementite globular and cementite lamellae particles within the fracture surface of both samples near the surface (with the dashed line). The cementite globular particles with a carbon concentration of 17.64 at.% (arrow in Fig. 14b) can act as a barrier to dislocation movement, which possibly contributes to the initial cyclic hardening for a few cycles at the low strain amplitude of 0.011 mm/mm; however, the cementite globular randomly dispersed in the small cluster region is unable to effectively oppose complex dislocation movement during strain cyclic deformation [13]. In addition, the small localized plastic strain and high stress concentrated in the martensite phase are believed to cause the rapid formation of microcracks [27]; thus, many sub-cracks are formed at the ferrite-martensite boundary, as shown in Fig. 14b, which accelerates crack propagation. Furthermore, cleavage facet-like features, which are caused by the

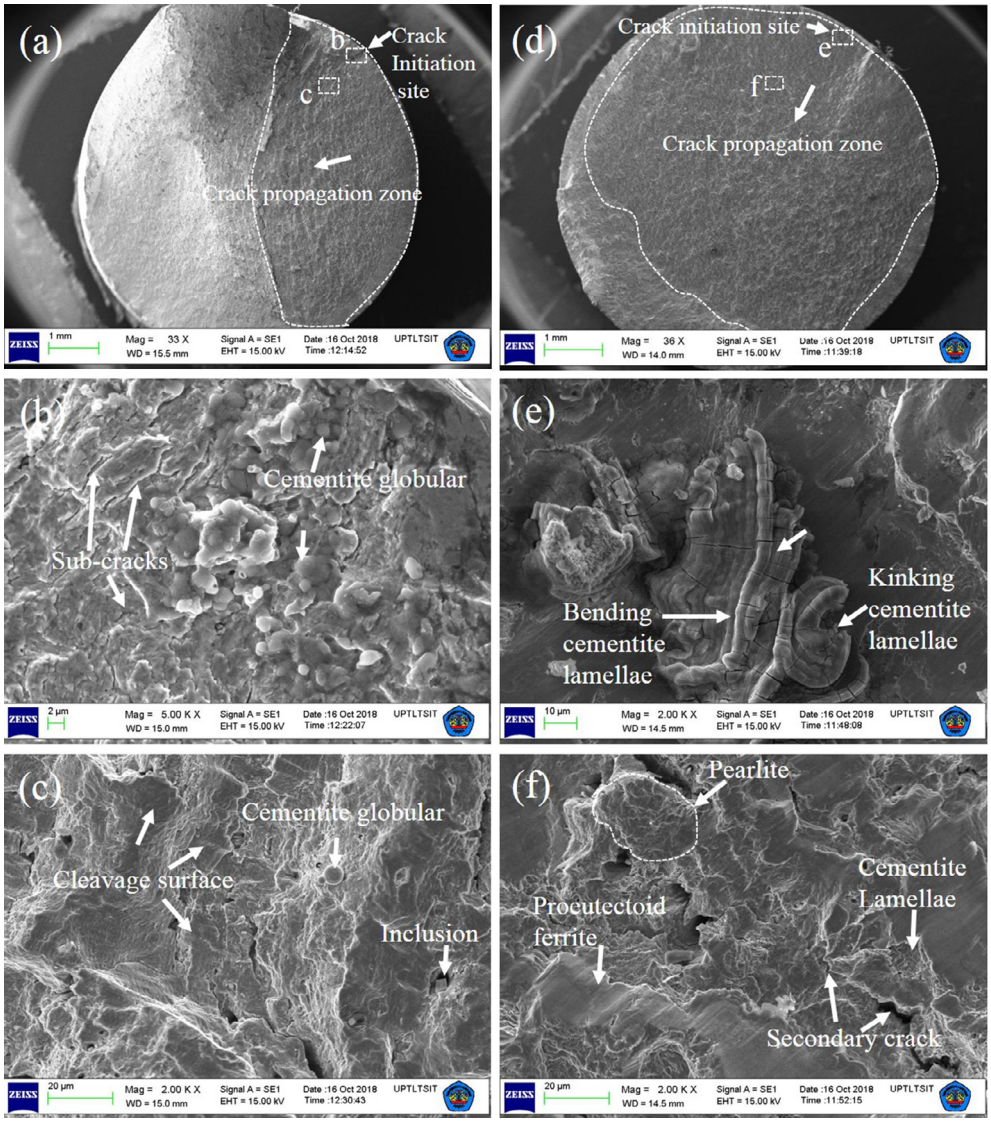

Fig. 14. SEM of fracture surfaces from the samples tested under LCF at a strain amplitude of 0.009 mm/mm; (a–c) the as-received AISI 4140 and (d–f) the AS.

shearing of the hard martensite phase and the restriction of the slip of the soft ferrite phase during cyclic straining fatigue, can be clearly seen in the fatigue propagation zone (Fig. 14c). The second phase of the inclusion particles, from which cracks initiate and propagate due to the relatively weak bonding of the particles with the matrix [34,39], is observed in Fig. 14c.

Energy dispersive spectroscopy (EDS) confirms that the cementite lamellae in the pearlite colonies has low carbon content (~14.3 at.%) (Fig. 14e). The bending and kinking of the lamellar shapes in Fig. 14e show that the carbide lamellar structure have a strong resistance to plastic deformation. The lamellar structure in the AS can resist dislocation motions effectively, thereby preventing dislocations in the ferrite; the surface fracture of the cementite lamellae exhibits decohesion due to stress build up around the ferrite matrix [40], which is evident in Fig. 14e. Furthermore, a flat fracture surface region with a low striation fatigue in the proeutectoid ferrite region is observed in Fig. 14f. In the coarse ferrite-pearlite microstructure, the ductile fracture crack growth is more dominated by pearlite colonies than by ferrite colonies, and pearlite colonies tend to retard crack growth [4,41]. Thus, several secondary cracks initiated and propagated at grain boundaries were observed in Fig. 14f. In the case of the annealed sample, the formation of the cementite lamellae was a result of decomposition of the carbon atoms, which led to the enhancement of the boundary cohesion and grain coarsening. The grain coarsening can trigger many dislocation motions in the grain interior, which leads to extensive plasticity at the crack tip before fracturing [42]. Therefore, the significant improvement in the LCF resistance of the AS is mainly due to the extensive work hardening that result from the highly plastic deformation of pearlite.

4. Conclusion

The initial cyclic hardening and progressive softening behaviour of AISI 4140 steel under Q&T conditions can be attributed to the initial microstructure of the steel, which consists of small ferrite grains and a fine martensite phase. The initial cyclic hardening is present at a low total strain amplitude of 0.009 mm/mm, and at higher total strain amplitudes, the steel exhibits progressive cyclic softening behaviour. In contrast, the ferrite-pearlite microstructure of AISI 4140 steel showed cyclic softening for a few cycles at a low total strain amplitude of 0.007 mm/mm and continuous cyclic hardening. With the increasing strain amplitude, cyclic hardening is observed. For all strain amplitudes > 0.003 mm/mm, the AISI 4140 steel under Q&T exhibits cyclic softening behaviour. In contrast, the AISI 4140 steel under annealing conditions transitions from softening behaviour to hardening behaviour at a total strain amplitude of 0.005 mm/mm, transitions from

hardening behaviour to softening behaviour at a total strain amplitude of 0.011 mm/mm, and exhibits near-Masing behaviour at the observed total strain amplitudes. The high fatigue strength coefficient (σ_f) and low fatigue strength exponent (b) of AISI 4140 under Q&T conditions indicate that the long life of the steel is dominantly controlled by the high elastic strain amplitude at a low strain amplitude of 0.003 mm/mm. However, for all total strain amplitudes, the annealed AISI 4140 steel displayed a greater LCF life than the quenched and tempered AISI 4140 steels.

The increase in the LCF resistance of the AISI 4140 steel under annealing conditions can be correlated with the low fatigue ductility exponent (c) and the high cyclic strain hardening exponent (n'). The small clusters of cementite globular and cementite lamellae found in the fracture surface of AISI 4140 steel under Q&T conditions and annealing conditions, respectively, exhibit different characteristics in terms of the fractural behaviour. The shearing in martensite and inclusions are believed to accelerate crack propagation in the quenched and tempered AISI 4140 steel. In contrast, the highly cyclic deformation of the cementite lamellae in the pearlite colonies significantly contributes to the improved LCF performance of the annealed AISI 4140 steel. In the present analysis, the effective and reliable alternative LCF prediction method using the Coffin-Manson approach suggests that AISI 4140 steel under annealing conditions can be a good choice for engineering components if LCF damage is considered.

Acknowledgements

The authors would like to thank Kemenristekdikti for providing financial support through the Directorate of Research and Community Service (DRPM) for the collaborative research and the international publication (PKLN) grant (contract No. 062/SP2H/LT/DRPM/2018). The authors also thank Mr. Sumaryo, S.T., for providing optical microscopy images from the Center for Science and Advanced Material Technology, National Nuclear Energy Agency of Indonesia.

References

[1] Krabiell A. Ulrich Reichel, Low-cycle fatigue properties of microalloyed medium carbon precipitation hardening steels in comparison to quenched and tempered steels. Steel Res Int 1993;64:425–30. https://doi.org/10.1002/srin.199301048.
[2] Thielen PN, Fine ME, Fournelle RA. Cyclic stress strain relations and strain-controlled fatigue of AISI 4140 steel. Acta Mater 1976;24:1–10. https://doi.org/10.1016/0001-6160(76)90140-1.
[3] Fatemi A, Zeng Z, Plaseied A. Fatigue behavior and life predictions of notched specimens made of QT and forged microalloyed steels. Int J Fatigue 2004;26:663–72. https://doi.org/10.1016/j.ijfatigue.2003.10.005.
[4] Sankaran S, Sarma VS, Padmanabhan KA. Low cycle fatigue behavior of a multiphase microalloyed medium carbon steel: comparison between ferrite – pearlite and quenched and tempered microstructures. Mater Sci Eng A 2003;345:328–35. https://doi.org/10.1016/S0921-5093(02)00511-7.
[5] Branco R, Costa JD, Antunes FV. Low-cycle fatigue behaviour of 34CrNiMo6 high strength steel. Theor Appl Fract Mech 2012;58:28–34. https://doi.org/10.1016/j.tafmec.2012.02.004.
[6] Paul SK, Stanford N, Hilditch T. Effect of martensite volume fraction on low cycle fatigue behaviour of dual phase steels: experimental and microstructural investigation. Mater Sci Eng A 2015;638:296–304. https://doi.org/10.1016/j.msea.2015.04.059.
[7] Paul SK, Stanford N, Hilditch T. Effect of martensite morphology on low cycle fatigue behaviour of dual phase steels: experimental and microstructural investigation. Mater Sci Eng A 2015;644:53–60. https://doi.org/10.1016/j.msea.2015.07.044.
[8] Singh V, Raju PVSS, Namboodhiri TKG, Rao PR. Low cycle fatigue behaviour of a low-alloy high-strength steel. Int J Fatigue 1990;12:289–92. https://doi.org/10.1016/0142-1123(90)90457-P.
[9] Plumbridge WJ, Bartlett RA. Cyclic response of a 1Cr – Mo – V low alloy steel. Int J Fatigue 1982;4:209–16. https://doi.org/10.1016/0142-1123(82)90003-2.
[10] Kang J, Zhang FC, Long XY, Lv B. Low cycle fatigue behavior in a medium-carbon carbide-free bainitic steel. Mater Sci Eng A 2016;666:88–93. https://doi.org/10.1016/j.msea.2016.03.077.
[11] Mediratta SR, Ramaswamy V, Rao PR. Influence of ferrite-martensite microstructural morphology on the low cycle fatigue of a dual-phase steel. Int J Fatigue 1985;7:107–15. https://doi.org/10.1016/0142-1123(85)90041-6.
[12] Lanzutti A, Pujatti M, Magnan M, Andreatta F, Nurmi H, Silvonen A, et al. Uniaxial fatigue properties of closed die hot forged 42CrMo4 steel: Effect of flash and mechanical surface treatments. Mater Des 2017;132:324–36. https://doi.org/10.1016/j.matdes.2017.07.017.
[13] Ye C, Suslov S, Kim BJ, Stach EA, Cheng GJ. Fatigue performance improvement in AISI 4140 steel by dynamic strain aging and dynamic precipitation during warm laser shock peening. Acta Mater 2011;59:1014–25. https://doi.org/10.1016/j.actamat.2010.10.032.
[14] Nagarajan VR, Putatunda SK. Influence of dissolved hydrogen on the fatigue crack growth behaviour of AISI 4140 steel. Int J Fatigue 2014;62:236–48. https://doi.org/10.1016/j.ijfatigue.2013.04.018.
[15] Soady KA, Mellor BG, West GD, Harrison G, Morris A, Reed PAS. Evaluating surface deformation and near surface strain hardening resulting from shot peening a tempered martensitic steel and application to low cycle fatigue. Int J Fatigue 2013;54:106–17. https://doi.org/10.1016/j.ijfatigue.2013.03.019.
[16] Zhou Q, Qian L, Meng J, Zhao L, Zhang F. Low-cycle fatigue behavior and microstructural evolution in a low-carbon carbide-free bainitic steel. Mater Des 2015;85:487–96. https://doi.org/10.1016/j.matdes.2015.06.172.
[17] Cieślak BA, Koralnik M, Kuziak R, Brynk T, Zygmunt T, Mizera J. Low-cycle fatigue behaviour and microstructural evolution of pearlitic and bainitic steels. Mater Sci Eng A 2019;747:144–53. https://doi.org/10.1016/j.msea.2019.01.043.
[18] Fatoba O, Akid R. Uniaxial cyclic elasto-plastic deformation and fatigue failure of API-5L X65 steel under various loading conditions. Theor Appl Fract Mech 2018;94:147–59. https://doi.org/10.1016/j.tafmec.2018.01.015.
[19] Matweb. < http://www.matweb.com/seacrh/QuickText.aspx?SearchText = AISI %204140 > . (accessed on 2 November 2017).
[20] ASTM E8M Standard test methods for tension testing of metallic materials. West Conshohocken, PA: ASTM International; 2016.
[21] ASTM E606-04 Standard practice for strain-controlled fatigue testing. West Conshohocken, PA: ASTM International; 2012.
[22] Sarkar PP, De PS, Dhua SK, Chakraborti PC. Strain energy based low cycle fatigue damage analysis in a plain C-Mn rail steel. Mater Sci Eng A 2017;707:125–35. https://doi.org/10.1016/j.msea.2017.09.035.
[23] Kwon H, Barlat F, Lee M, Chung Y, Uhm S. Influence of tempering temperature on low cycle fatigue of high strength steel. ISIJ Int 2014;54:979–84. https://doi.org/10.2355/isijinternational.54.979.
[24] Zhu Z, Lu Y, Xie Q, Li D, Gao N. Mechanical properties and dynamic constitutive model of 42CrMo steel. Mater Des 2017;119:171–9. https://doi.org/10.1016/j.matdes.2017.01.066.
[25] Hwang BC, Cao TY, Shin SY, Kim SH, Lee SH, Kim SJ. Effects of ferrite grain size and martensite volume fraction on dynamic deformation behaviour of 0.15C–2.0Mn–0.2Si dual phase steels. Mater Sci Technol 2005;21:967–75. https://doi.org/10.1179/174328405X47609.
[26] Tsuchida N, Tomota Y, Nagai K, Fukaura K. A simple relationship between Lu¨ders elongation and work-hardening rate at lower yield stress. Scrip Mater 2006;54:57. https://doi.org/10.1016/j.scriptamat.2005.09.011.
[27] Zhang J, Di H, Deng Y, Misra RDK. Effect of martensite morphology and volume fraction on strain hardening and fracture behavior of martensite–ferrite dual phase steel. Mater Sci Eng A 627 2015:230–40. https://doi.org/10.1016/j.msea.2015.01.006.
[28] Kunc R, Prebil I. Low-cycle fatigue properties of steel 42CrMo4. Mater Sci Eng A 2003;345:278–85. https://doi.org/10.1016/S0921-5093(02)00464-1.
[29] Sarma VS, Padmanabhan KA, Das S. Transmission electron microscopy of a cyclically deformed medium carbon microalloyed steel. J Mater Sci Lett 1997;16:1495–8. https://doi.org/10.1023/A:1018562822420.
[30] Yang L, Gao Y, Shi G, Wang X, Bai Y. Low cycle fatigue property and fracture behavior of low yield point steels. Const Build Mater 2018;165:688–96. https://doi.org/10.1016/j.conbuildmat.2018.01.075.
[31] Kreethi R, Mondal AK, Dutta K. Ratcheting fatigue behaviour of 42CrMo4 steel under different heat treatment conditions. Mater Sci Eng A 2017;679:66–74. https://doi.org/10.1016/j.msea.2016.10.019.
[32] Sarkar A, Kumawat BK, Chakravartty JK. Low cycle fatigue behavior of a ferritic reactor pressure vessel steel. J Nucl Mater 2015;462:273–9. https://doi.org/10.1016/j.jnucmat.2015.04.015.
[33] Chakraborti PC, Mitra MK. Room temperature low cycle fatigue behaviour of two high strength lamellar duplex ferrite–martensite (DFM) steels. Int J Fatigue 2005;27:511–8. https://doi.org/10.1016/j.ijfatigue.2004.09.003.
[34] Tartaglia JM, Hayrynen KL. A comparison of fatigue properties of austempered versus quenched and tempered 4340 steel. JMEPEG 2012;21:1008–24. https://doi.org/10.1007/s11665-011-9951-y.
[35] Shiozaki T, Tamai Y, Urabe T. Effect of residual stresses on fatigue strength of high strength steel sheets with punched holes. Int J Fatigue 2015;80:324–31. https://doi.org/10.1016/j.ijfatigue.2015.06.018.
[36] Roessle ML, Fatemi A. Strain-controlled fatigue properties of steels and some simple approximations. Int J Fatigue 2000;22:495–511. https://doi.org/10.1016/S0142-1123(00)00026-8.
[37] Nikitin I, Besel M. Correlation between residual stress and plastic strain amplitude during low cycle fatigue of mechanically surface treated austenitic stainless steel AISI 304 and ferritic–pearlitic steel SAE 1045. Mater Sci Eng A 2008;491:297–303. https://doi.org/10.1016/j.msea.2008.03.034.
[38] Lefebvre D, Ellyin F. Cyclic response and inelastic strain energy in low cycle fatigue. Int J Fatigue 1984;6:9–15. https://doi.org/10.1016/0142-1123(84)90003-3.
[39] Jordon JB, Horstemeyer MF. Microstructure-sensitive fatigue modeling of AISI 4140 steel. J Eng Mater Technol 2014;136(2):021004. https://doi.org/10.1115/1.4025424.
[40] Zhou L, Fang F, Wang L, Chen H, Jiang J. Torsion delamination and recrystallized cementite of heavy drawing pearlitic wires after low temperature annealing. Mater Sci Eng A 2018;713:52–60. https://doi.org/10.1016/j.msea.2017.12.055.

[41] Lee JW, Lee JC, Lee YS, Park KT, Nam WJ. Effects of post-deformation annealing conditions on the behavior of lamellar cementite and the occurrence of delamination in cold drawn steel wires. J Mater Proces Technol 2009;209:5300–4. https://doi.org/10.1016/j.jmatprotec.2009.03.019.

[42] Jaya BN, Goto S, Richter G, Kirchlechner C, Dehm G. Fracture behavior of nanostructured heavily cold drawn pearlitic steel wires before and after annealing. Mater Sci Eng A 2017;707:164–71. https://doi.org/10.1016/j.msea.2017.09.010.